nature communications

Article

https://doi.org/10.1038/s41467-025-61611-6

Finite-time scaling beyond the Kibble-Zurek prerequisite in Dirac systems

Received: 11 September 2024

Accepted: 25 June 2025

Published online: 04 July 2025

Check for updates

Zhi Zeng[1,2,5], Yin-Kai Yu[1,2,3,4,5], Zhi-Xuan Li[1,2,5], Zi-Xiang Li[3,4] ✉ & Shuai Yin[1,2] ✉

The conventional Kibble-Zurek mechanism and the finite-time scaling provide universal descriptions of the driven critical dynamics from gapped initial states based on the adiabatic-impulse scenario. Here we investigate the driven critical dynamics in two-dimensional Dirac systems, which harbor semimetal and Mott insulator phases separated by the quantum critical point triggered by the interplay between fluctuations of gapless Dirac fermions and order parameter bosons. We find that despite the existence of the gapless initial phase, the driven dynamics can still be captured by the finite-time scaling form. This leads us to propose a criterion for the validity of Kibble-Zurek mechanism with a gapless initial state. Accordingly, our results generalize the Kibble-Zurek theory to incorporate composite fluctuations and relax its requirement for a gapped initial state to systems accommodating gapless Dirac fermionic excitations. Our work not only brings fundamental perspective into the nonequilibrium critical dynamics, but also provides an approach to fathom quantum critical properties in fermionic systems.

Fathoming nonequilibrium universal properties near a quantum critical point (QCP) is one of the central issues in modern physics[1,2]. Although the general organizing principle for the nonequilibrum critical dynamics is still elusive, a unified framework for understanding the generation of topological defects after the linear quench was proposed by Kibble in cosmological physics and then generalized by Zurek in condensed matter systems[3,4]. This celebrated Kibble-Zurek mechanism (KZM) has aroused intensive investigations from both theoretical and experimental aspects, exerting far-reaching significance in both classical and quantum phase transitions[3–16]. More interestingly, it was found that scaling behaviors can also manifest themselves in the driven process[17–21]. As a generalization of the KZM, a finite-time scaling (FTS) theory was proposed to systematically understand the full scaling properties[22,23]. These full scaling forms have been verified in various systems from numerical to experimental works[11,12,20,22–29]. Moreover, the KZM and the FTS recently show their fabulous power in state preparations and probing critical properties in fast-developing programmable quantum devices[11,12,28–30].

At the core of the original KZM lies the adiabatic-impulse scenario[1,2,31]. According to it, a crucial prerequisite for the implementation of the KZM is the existence of a gapped initial stage, wherein the system evolves adiabatically along the equilibrium state. The border of this initial stage with the intrinsically nonequilibrium impulse region gives rise to a frozen time[1–4], which dominates the critical dynamics near the critical point, yielding the FTS forms[22,23]. Moreover, intriguing dynamic scaling behavior dominated by the QCP was also found for driven dynamics from gapless initial phase to cross the QCP in one dimensional spin systems[32,33]. However, the universal criterion for the validity of KZM and FTS with a gapless initial state has yet to be established.

The QCP occurring in strongly interacting Dirac systems, dubbed as Dirac QCP, represents a typical class of QCP which has joint critical fluctuations from both order parameter and gapless fermions. Studies

[1]Guangdong Provincial Key Laboratory of Magnetoelectric Physics and Devices, School of Physics, Sun Yat-Sen University, Guangzhou 510275, China. [2]School of Physics, Sun Yat-Sen University, Guangzhou 510275, China. [3]Beijing National Laboratory for Condensed Matter Physics & Institute of Physics, Chinese Academy of Sciences, Beijing 100190, China. [4]University of Chinese Academy of Sciences, Beijing 100049, China. [5]These authors contributed equally: Zhi Zeng, Yin-Kai Yu, Zhi-Xuan Li. ✉e-mail: zixiangli@iphy.ac.cn; yinsh6@mail.sysu.edu.cn

of Dirac QCP stem from the research in modern high-energy physics, such as chiral symmetry in QCD and mass generation via spontaneous symmetry breaking[34–37]. From the perspectives of statistical mechanics and condensed matter physics, the Dirac QCP also attracts enormous attentions, particularly after the experimental realization of two-dimensional Dirac fermions in graphene and various topological insulators or semimetals[38–40]. The presence of Dirac fermions is theoretically revealed to tremendously enrich quantum critical properties, rendering novel universality classes of quantum phase transition without classical counterpart[41–52].

Interesting aspects of Dirac QCP in equilibrium can suggest interesting phenomena out of equilibrium. Dynamic scaling behaviors were studied in QCPs that feature non-interacting Dirac fermions[53–55]. However, nonequilibrium dynamics in strongly interacting Dirac QCP is still largely unexplored. Particularly, for driven dynamics along the gapless Dirac semimetal (DSM) phase to cross the QCP, whether the original KZM is still applicable remains unknown. Consequently, investigating the nonequilibrium driven dynamics in Dirac QCP has overarching meaning in fundamental theory, as well as immediate applications in the context of detecting and exploring fermionic QCP in experimental platforms[38–40].

However, directly tackling the real-time dynamics in two or higher spatial dimension is largely hindered by the lack of reliable theoretical or numerical methods. Specifically, quantum Monte Carlo (QMC) fails as a result of the notorious sign problem[56,57], while the tensor-network method still needs tremendous improvements despite remarkable progress in recent years[58]. Fortunately, scaling analysis demonstrates that both real- and imaginary-time driven dynamics share the same scaling form[59] as elucidated in Supplementary Note 1. This inference has been verified in various systems[27,28,59], bridging the gap between the QMC imaginary-time simulations without sign problem and the real-time dynamics as discussed in Supplementary Note 2.

In this work, we investigate the driven critical dynamics of two representative strongly interacting Dirac QCPs, belonging to chiral Heisenberg and chiral Ising universality classes, respectively, via the determinant QMC method[56]. By linearly varying the interaction strength along the imaginary-time direction to cross the QCP from both the DSM and Mott insulator phases, we uncover that the driven process near the Dirac QCP satisfies the scaling form of FTS despite the violation of the adiabatic-impulse scenario of the KZM due to the existence of the gapless initial state. Furthermore, we develop a universal criterion for the validity of the KZM and FTS with the gapless initial state. In addition, our numerical simulation achieves the critical exponents of the Dirac QCP, whose values obtained in previous studies on equilibrium properties are still under debate. Through the generalization of quantum driven critical dynamics to strongly interacting Dirac QCP, our study not only leads to an extension of the fundamental theory of KZM and FTS, but also contributes a feasible approach to investigate the fermionic quantum critical phenomena in realistic platform such as quantum materials and devices.

RESULTS

Dynamics in chiral Heisenberg criticality

A typical model hosting Dirac QCP belonging to chiral Heisenberg universality class is the Hubbard model on the half-filled honeycomb lattice with the Hamiltonian[42,46–49]

$$H = -t\sum_{\langle ij\rangle,\sigma} c^{\dagger}_{i\sigma}c_{j\sigma} + U\sum_{i}\left(n_{i\uparrow}-\frac{1}{2}\right)\left(n_{i\downarrow}-\frac{1}{2}\right), \tag{1}$$

in which $c^{\dagger}_{i\sigma}$ ($c_{j\sigma}$) represents the creation (annihilation) operator of electrons with spin σ, $n_{i\sigma}\equiv c^{\dagger}_{i\sigma}c_{i\sigma}$ is the electron number operator, t is the hopping amplitude between nearest neighbor sites and set as the energy unit in the following, and U is the strength of the on-site repulsive interaction. The model is absent from sign problem in QMC simulation as discussed in Supplementary Note 2. As shown in Fig. 1, a critical point $U_c \approx 3.85$ separates two phases[49]. When $U > U_c$, the system is in the antiferromagnetic (AFM) Mott insulator phase in which fermions acquire a mass originating from spontaneous symmetry breaking characterized by the finite AFM order parameter $m^2 = \sum_{i,j}\eta_i\eta_j\langle S^z_i S^z_j\rangle/L^{2d}$ with $S^z_i \equiv (1/2)\mathbf{c}^{\dagger}_i\sigma^z\mathbf{c}_i$, $\mathbf{c} \equiv (c_\uparrow, c_\downarrow)$, and $\eta_i = \pm 1$ for $i \in A(B)$ sublattice[42,48,49]. Here, L is the linear size of the system and $d = 2$ is the spatial dimension. In this phase, the transverse spin excitation is massless due to the presence of the Goldstone modes. In contrast, when $U < U_c$, the system is in the DSM phase with four-component massless Dirac fermion ($N_f = 2$). At U_c, both Dirac fermions and AFM order parameter bosons are gapless, yielding the Gross-Neveu QCP belonging to chiral Heisenberg universality class[42,46–49].

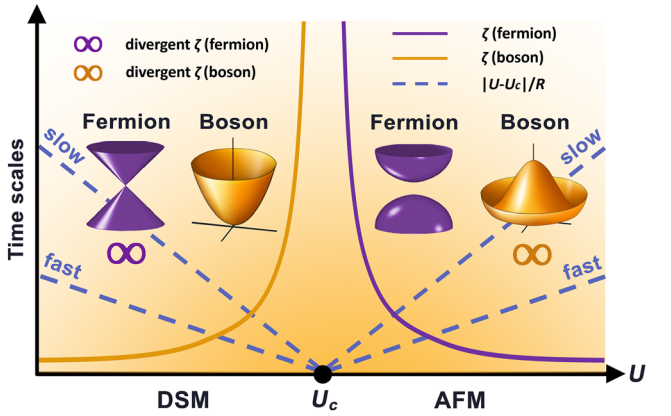

Fig. 1 | Time scales for driven critical dynamics. The quantum critical point at U_c separates the Dirac semimetal (DSM) phase featured by the fermionic Dirac cone (violet cone) and massive bosonic modes (golden paraboloid) from the antiferromagnetic (AFM) phase featured by the massive fermionic excitation (violet hyperbolic paraboloid) and massless bosonic modes (golden Mexican hat). The gradient yellow background around U_c indicates the critical region. The correlation time scales ζ for both boson (yellow solid curve) and fermion (violet solid curve) are finite in one phase but divergent (symbolized by "∞") in the other phase. The dashed line denotes the time distance $|U - U_c|/R$ to the critical point for different driving rates. Accordingly, the prerequisite of the original KZM that a gapped initial state should exist to protect an initial adiabatic stage, in which the transition time is larger than the correlation time, breaks down.

Here we begin to explore whether the FTS forms are still applicable in the driven dynamics of this Dirac QCP with composite critical fluctuations from gapless initial states. First we study the driven dynamics by varying U with imaginary time τ as $U = U_0 + R\tau$ from the DSM initial state with $U_0 = 0$, as illustrated in Fig. 1. We denote the distance to the critical point as g (here $g = U - U_c$). The smallest lattice size is chosen as $L = 18$ to eliminate the scaling violation induced by small sizes. When $g = 0$, from Fig. 2a, we find that for large R, $m^2 \propto L^{-2}R^{-0.26(1)}$ with the exponent on R close to $(2\beta - d\nu)/\nu r = -0.26(2)$, in which $\beta = 0.76(2)$ and $\nu = 1.02(1)$ are the exponents for order parameter and correlation length, respectively[49], and $r = z + 1/\nu$ is the scaling dimension of R. Here the dynamic exponent z equals one in the Gross-Neveu Dirac QCP owing to the Lorentz symmetry of the effective model[47]. Additionally, the exponent on R is almost independent of L. In contrast, when R is small, Fig. 2a shows that m^2 tends to saturate and the usual finite-size scaling $m^2 \propto L^{-2\beta/\nu}$ is restored. To reconcile these rescaling relations, the scaling form must satisfy

$$m^2(R, L, g) = L^{-d}R^{(2\beta - d\nu)/\nu r}\mathcal{F}(RL^r, gL^{1/\nu}), \tag{2}$$

in which $\mathcal{F}$ is a non-singular scaling function and therein dimensionless quantity $gL^{1/\nu}$ is also included to take account of the off-critical-point effects. Eq. (2) is consistent with the FTS in conventional bosonic QCP[24,25].

https://doi.org/10.1038/s41467-025-61611-6

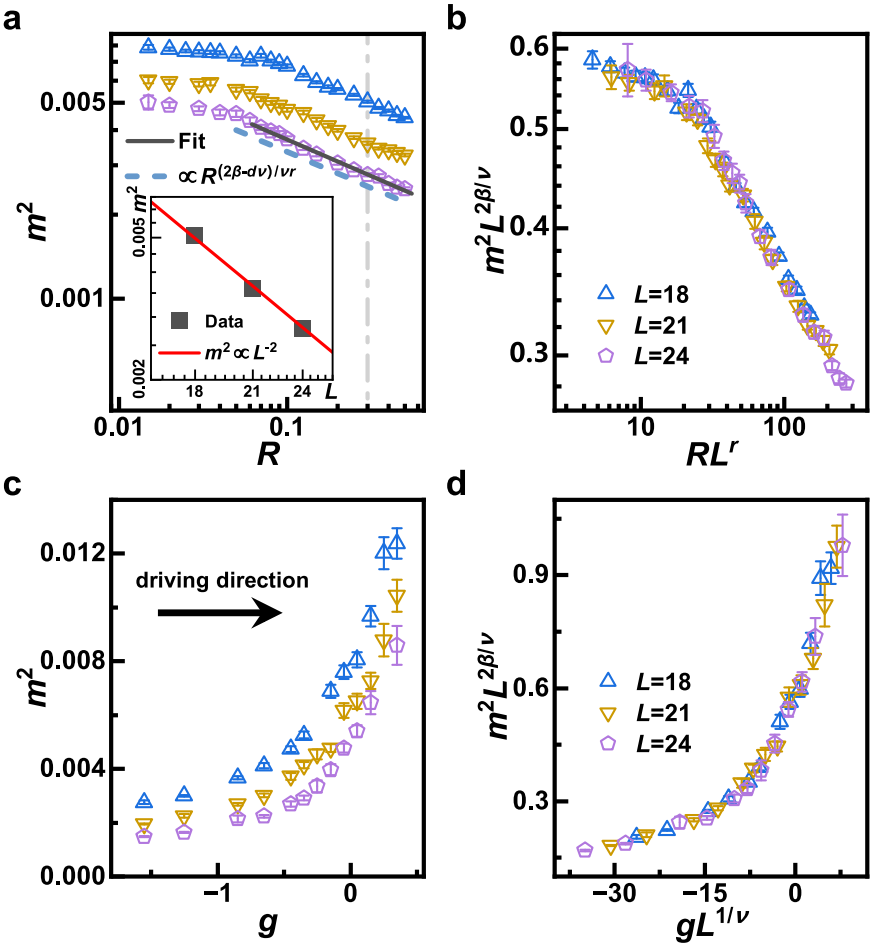

Fig. 2 | Driven dynamics from the DSM phase of model (1). a, **b** are log-log plots of m^2 versus R for different L driven to $U_c = 3.85$ before and after rescaling. Inset in (**a**) shows $m^2 \propto L^{-2}$ for $R = 0.3$ (dash-dotted line). For large R, power fitting for $L = 24$ (black solid line) shows $m^2 \propto R^{-0.26(1)}$ with the exponent close to $(2\beta - d\nu)/\nu r = -0.26(2)$ (dash line) from ref. 49. **c**, **d** are curves of m^2 versus g for fixed $RL^r = 5.41$ and different L before and after rescaling. The arrow indicates the driving direction. The errorbars represent one standard deviation.

To confirm Eq. (2), we find that Eq. (2) yields the scaling form $m^2(R,L) = L^{-2\beta/\nu}\mathcal{F}_1(RL^r)$ at $g = 0$. Here, we rescale m^2 and R as $m^2L^{2\beta/\nu}$ and RL^r with the exponents $\beta = 0.76(2)$, $\nu = 1.02(1)$[49], and $z = 1$[47] set as input, and reveal that the rescaled curves collapse well into a single curve, as shown in Fig. 2b, confirming Eq. (2) at $g = 0$.

In addition, to unravel the scaling properties in the driven process near U_c, we calculate the dependence of m^2 on g for an arbitrary fixed $RL^r = 5.41$ and present the results in Fig. 2c. After rescaling m^2 and g by $L^{2\beta/\nu}$ and $L^{1/\nu}$, the curves with various L collapse into each other, as displayed in Fig. 2d, confirming that the universal scaling behavior of physical observable in the driven process is described by Eq. (2).

The reason for the appearance of the scaling relation $m^2 \propto L^{-d}R^{(2\beta-d\nu)/\nu r}$ is that for large R, driven induced length scale $\xi_R \sim R^{-1/r}$ is smaller than L. Thus, the definition of m^2 indicates that $m^2 \propto L^{-d}$ owing to the central limit theorem. Meanwhile, the rest part of the dimension of m^2 should be borne by R, giving rise to the leading term of Eq. (2). In this case, $\mathcal{F}(RL^r, 0)$ tends to a constant. In contrast, for small R, $\xi_R > L$, such that the conventional finite-size scaling at equilibrium $m^2 \propto L^{-2\beta/\nu}$ is recovered, and $\mathcal{F}(RL^r, 0)$ obeys $\mathcal{F}(RL^r, 0) \sim (RL^r)^{d/r-2\beta/\nu r}$.

Next, we turn to explore the driven dynamics starting from the Mott insulator initial state and U is changed as $U = U_0 - R\tau$ with $U_0 = 11.85$. This Mott insulator state has the AFM order with transverse gapless modes. For large R, Fig. 3a shows that $m^2 \propto R^{0.73(2)}$ with the exponent close to $2\beta/\nu r = 0.75(2)$[49] and is nearly independent of L. Combining this scaling relation with the usual finite-size scaling $m^2 \propto L^{-2\beta/\nu}$ which is restored for small R, the scaling form should obey

$$m^2(R,L,g) = R^{2\beta/\nu r}\mathcal{G}(RL^r, gL^{1/\nu}), \tag{3}$$

where $\mathcal{G}$ is the scaling function and g is also included therein. Eq. (3) is also accordant with the conventional FTS with ordered initial state[22–24].

We rescale curves of m^2 versus R for various L at $g = 0$ according to the scaling function $m^2(R,L) = L^{-2\beta/\nu}\mathcal{G}_1(RL^r)$ and find that the rescaled curves collapse well, which confirms Eq. (3) at $g = 0$. Note that in Fig. 3b slight deviation appears in the large R region, which may stem from the influence of high-energy modes caused by fast driving. Furthermore, Fig. 3c shows the curves of m^2 versus g for an arbitrary fixed RL^r. The rescaled results ($gL^{1/\nu}$, $m^2L^{2\beta/\nu}$) for various L collapse into a single smooth curve, as displayed in Fig. 3d, confirming that the driven process from AFM initial state is described by Eq. (3).

The appearance of $m^2 \propto R^{2\beta/\nu r}$ reflects the fact that when $\xi_R < L$ the initial ordered magnetization domain is maintained. In this case, $\mathcal{G}(RL^r, 0)$ in Eq. (3) tends to a constant and $\mathcal{G}_1(RL^r) \sim (RL^r)^{2\beta/\nu r}$. In contrast, for small R with $\xi_R > L$, the usual finite-size scaling $m^2 \propto L^{-2\beta/\nu}$ is recovered, indicating that $\mathcal{G}(RL^r, 0) \sim (RL^r)^{-2\beta/\nu r}$ and $\mathcal{G}_1(RL^r)$ tends to a constant.

Dynamics in chiral Ising criticality

To further verify the FTS in Dirac systems, we also explore the driven dynamics of Dirac QCP belonging to chiral Ising universality class, which is realized in the interacting spinless fermion model on the

https://doi.org/10.1038/s41467-025-61611-6

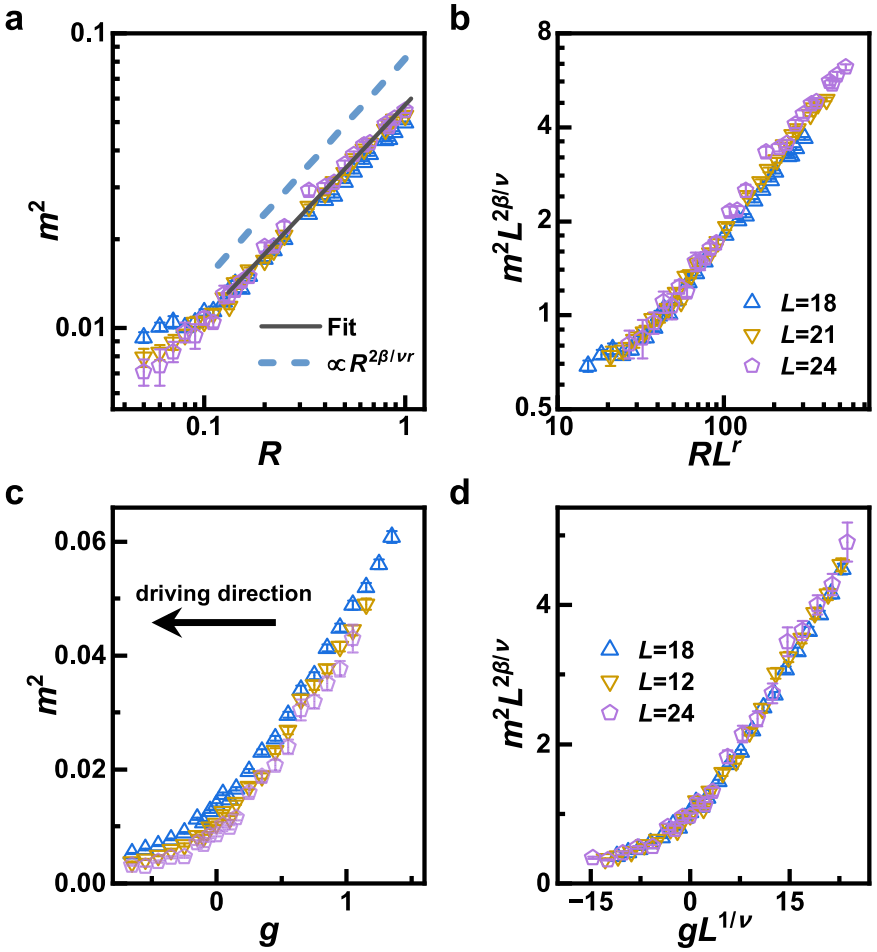

Fig. 3 | Driven dynamics from the AFM phase of model (1). a, b are log-log plots of m^2 versus R for different L driven to $U_c = 3.85$ before and after rescaling. For large R, power fitting (black solid line) shows $m^2 \propto R^{0.73(2)}$ with the exponent close to $2\beta/\nu r = 0.75(2)$ (dash line) from ref. 49. **c, d** are curves of m^2 versus g for fixed $RL^r = 41.5$ and different L before and after rescaling. The arrow indicates the driving direction. The errorbars represent one standard deviation.

half-filled honeycomb lattice with the Hamiltonian[50,51,60]:

$$H = -t\sum_{\langle ij\rangle} c_i^\dagger c_j + V\sum_{\langle ij\rangle}\left(n_i - \frac{1}{2}\right)\left(n_j - \frac{1}{2}\right), \tag{4}$$

where V measures the nearest-neighbor interaction. The model is amendable to sign-problem-free QMC simulation as discussed in Supplementary Note 2[61–63]. It was shown that the ground state undergoes a continuous quantum phase transition at $V_c \approx 1.355$ from the DSM phase to the charge-density-wave (CDW) insulator phase, characterized by the order parameter $m^2 \equiv \sum_{i,j}\eta_i\eta_j\langle(n_i - 1/2)(n_j - 1/2)\rangle/L^{2d}$ with $\eta_i = \pm 1$ for $i \in A(B)$ sublattice[50,51,60]. At $V = V_c$, both fermion and boson degrees of freedom are gapless, similar to model (1). However, a difference is that in the CDW phase, the bosonic fluctuation is fully gapped owing to the discrete symmetry breaking.

For the driven dynamics under changing V as $V = V_0 + R\tau$ from the DSM initial state with $V_0 = 0$, Figure 4a shows that at $g = 0$, for large R, $m^2 \propto L^{-2}R^{-0.336(4)}$ with the exponent on R close to $(2\beta - d\nu)/\nu r = -0.31(4)$ in which $\beta = 0.47(4)$, $\nu = 0.74(4)$[60], and $z = 1$[64]; whereas $m^2 \propto L^{-2\beta/\nu}$ for small R, similar to the results in model (1). In addition, we find the rescaled curves of m^2 versus R and g collapse well, as shown in Fig. 4b, d, confirming that Eq. (2) gives a universal description on the driven critical dynamics from the DSM initial state.

For the driven dynamics under changing V as $V = V_0 - R\tau$ from the CDW initial state with $V_0 = 2.5$, Fig. 5a shows that at $g = 0$, for large R, $m^2 \propto R^{0.496(6)}$ with the exponent close to $2\beta/\nu r = 0.54(4)$[60], whereas $m^2 \propto L^{-2\beta/\nu}$ for small R, similar to the case of chiral Heisenberg universality class. Moreover, Eq. (3) is verified by the data collapse of the curves $(RL^r, m^2L^{-2\beta/\nu})$ at fixed $g = 0$ and $(gL^{1/\nu}, m^2L^{-2\beta/\nu})$ for an arbitrary RL^r, as shown in Fig. 5b, d. Consequently, Eq. (3) provides a universal description on the driven dynamics from ordered initial states, regardless of whether or not initial gapless bosonic modes exist.

General scaling theory

The above numerical results remarkably demonstrate that the FTS forms are applicable despite the existence of gapless initial states which can violate the adiabatic-impulse scenario of the original KZM. Thus, it is imperative to develop a universal scaling scenario.

In driven dynamics starting from a ground state far from the critical point, the driving rate R uniquely quantifies the extent of departure from the equilibrium state. Within the original KZM, the existence of an initial adiabatic stage stabilized by a finite gap can remarkably suppress excitations triggered by external driving[1,2,31]. This leads to the fact that the excitations are predominantly generated near the QCP. Consequently, the dimension of the driving rate R, namely r, is exclusively determined by the critical exponents of the QCP, forming the basis for the original KZM and FTS.

In contrast, at first sight, for the driven dynamics evolving along a gapless initial stage and then crossing the QCP, the excitations can also be copiously produced in the initial gapless phase and subsequently brought into the critical region to influence the nonequilibrium properties near the QCP. Accordingly, we can formulate a scale

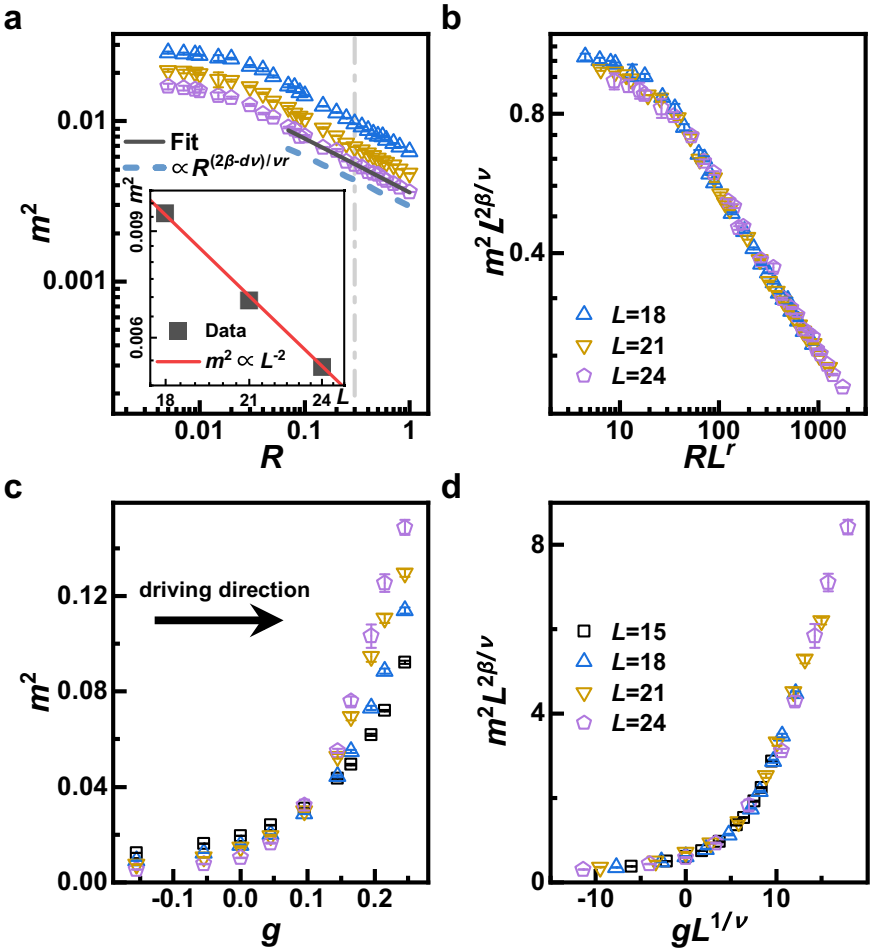

Fig. 4 | Driven dynamics from the DSM phase of model (4). a, **b** are log-log plots of m^2 versus R for different L driven to $V_c = 1.355$ before and after rescaling. Inset in (**a**) shows $m^2 \propto L^{-2}$ for $R = 0.3$ (dash-dotted line). For large R, power fitting for $L = 24$ (black solid line) shows $m^2 \propto R^{-0.336(4)}$ with the exponent close to $(2\beta - d\nu)/\nu r = -0.31(4)$ (dash line) from ref. 60. **c**, **d** are curves of m^2 versus g for fixed $RL^r = 63.34$ and different L before and after rescaling. The arrow indicates the driving direction. The errorbars represent one standard deviation.

transformation under which a macroscopic quantity Q should transform as

$$Q(R, g, L, Q_0; R') = b^{-\kappa} Q(Rb^r, gb^{1/\nu}, Lb^{-1}, Q_0 b^{\kappa_0}; R' b^{r'}), \tag{5}$$

in which b ($b > 1$) is the rescaling factor, κ is the scaling dimension of Q, and R' along with its exponent r' characterizes the contribution from the excitations generated in the gapless initial stage. Note that although the value of R' is equal to that of R, in general, they can have different scaling dimensions. Specifically, r' is dictated by the exponent of the gapless phase; whereas r is determined by the exponent of the QCP. In addition, in Eq. (5), Q_0 and κ_0 represent the initial value of Q and its scaling dimension, respectively. From Eq. (5), one finds that when $r' < r$, the nonequilibrium dynamics across the QCP is governed R with dimension r and the usual KZM and FTS can be restored.

Moreover, in practice, the condition can be further refined. Since the gapless phase can be viewed as a continuous set of critical points belonging to the same universality class, its stability requires that the tuning parameter Λ [for example, U or V in the DSM phase in models (1) and (4), respectively] must be either irrelevant or at most marginally irrelevant. More precisely, under a scale transformation with a coarse graining factor b ($b > 1$), Λ changes as $\Lambda \to \Lambda b^{\lambda}$ with $\lambda \leq 0$. Applying this scaling to a change in the tuning parameter, $\Delta\Lambda = R/\Delta t$, we obtain $\Delta\Lambda b^{\lambda} = R' b^{r'} \Delta t b^{-z'}$. This leads to the relation $r' = \lambda + z'$, where z' is the dynamic exponent of the gapless phase (which may differ from z characterizing QCP). Hence, $r' \leq z'$ because $\lambda \leq 0$, with equality holding for the marginally irrelevant case.

Consequently, we arrive at the precondition under which the usual KZM and FTS can be recovered for the gapless initial state,

$$z' < r, \ r = z + \frac{1}{\nu}. \tag{6}$$

Should Eq. (6) be met, the preponderant nonequilibrium universal behaviors will originate from the critical region of QCP because $r' < r$, and R with exponent r will govern the dynamic scaling behaviors, while the variable R' can be neglected in Eq. (5). To illustrate this, we consider the scaling of m^2. By setting the coarse-graining factor to $b = R^{-1/r}$ in Eq. (5), we can transform Eq. (5) into,

$$m^2(R, g, L, m_0^2) = m_0^2 R^{2\beta/\nu r - x_0/r} \mathcal{K}(gR^{-1/\nu r}, LR^{1/r}), \tag{7}$$

The scaling function $\mathcal{K}(gR^{-1/\nu r}, LR^{1/r})$ can be equivalently rewritten as $\mathcal{K}_1(gL^r, LR^{1/r})$. For the ordered initial state, m_0^2 approaches a saturation value, and $x_0 = 0$. In this case, Eq. (7) reduces to Eq. (3), thus recovering the expected scaling. In contrast, for the DSM initial state, since $m_0^2 \propto L^{-d}$, $x_0 = d$ and Eq. (7) recovers Eq. (2).

Now we apply the general discussion elaborated above to the models we are currently dealing with.

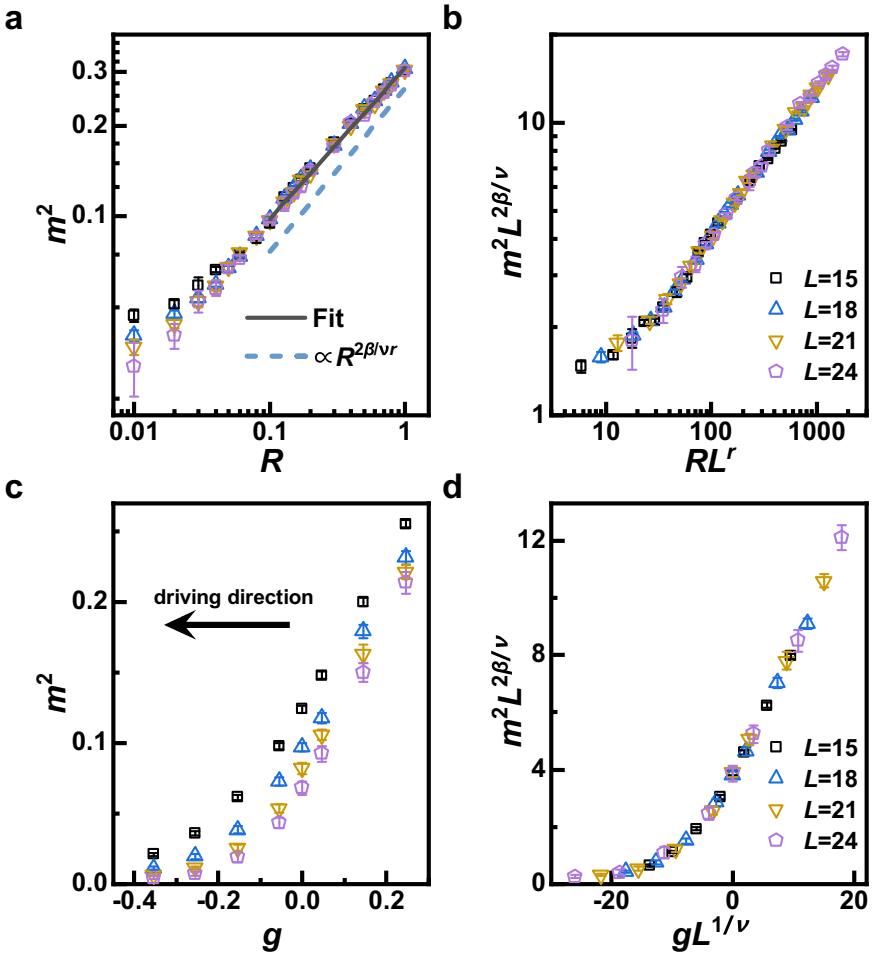

Fig. 5 | Driven dynamics from the CDW phase of model (4). a, **b** are log-log plots of m^2 versus R for different L driven to $V_c = 1.355$ before and after rescaling. For large R, power fitting (black solid line) shows $m^2 \propto R^{0.496(6)}$ with the exponent close to $2\beta/\nu r = 0.54(4)$ from ref. 60 (dash line). **c**, **d** are curves of m^2 versus g for fixed $RL^r = 87.97$ and different L before and after rescaling. The arrow indicates the driving direction. The errorbars represent one standard deviation.

- For driven dynamics from the DSM phase, as illustrated in Fig. 1, the DSM phase is characterized by low-energy physics dominated by the fermion fluctuations exhibiting linear dispersion, $E_k = v_f|k|^{z'}$, where $z' = 1$ and v_f represents the fermion velocity. Given that in the DSM phase $z' = 1$, Eq. (6) is apparently fulfilled. Consequently, the nonequilibrium dynamics across the QCP should be described by the standard FTS form.
- For driven dynamics from the AFM phase, in the AFM phase, the Dirac fermions feature a gap related to the amplitude of the AFM order parameter, and the low-energy excitations are predominantly attributed to bosonic spin waves, which correspond to the gapless Goldstone modes due to the broken spin rotation symmetry. The AFM spin wave has the linear dispersion as $E_k = v_b|k|^{z'}$, where $z' = 1$ and v_b denotes the spin wave velocity. Again, Eq. (6) is satisfied and the standard FTS form should be recovered.

Physically, in both DSM and AFM phases, different interaction strengths just yield different low-energy excitation velocity, but do not change the linear form of low-energy dispersion[65]. Therefore, the interaction strength are marginally irrelevant and the dimension of R' reduces to $z' = 1$. In contrast, in the critical region of the QCP, with the onset of ordering of the bosonic order parameter fields, both the bosonic and fermionic degrees of freedom evolve into the low-energy excitations. Apart from the remarkable proliferation of low-energy modes, the mutual interactions among them trigger intrinsic changes in the scaling dimensions of both Dirac fermion and order parameter, rather than merely adjusting v_f and v_b. In this case, U in model (1) [or V in model (4)] becomes relevant and $(U - U_c)$ in model (1) [or $(V - V_c)$ in model (4)] has the dimension of $1/\nu$. Consequently, R with dimension r is more relevant than R'.

DISCUSSION

In summary, we investigate the driven dynamics of QCP in two representative interacting Dirac-fermion systems, belonging to chiral Heisenberg and chiral Ising universality classes, respectively, through sign-problem-free QMC simulation. Driving the system from both DSM and Mott insulator phases as the initial states, we discover varieties of interesting nonequilibrium scaling behaviors. Furthermore, we confirm that these scaling behaviors can be unified by the full scaling form of the FTS theory.

From the theoretical perspectives, through this work we not only successfully generalize the KZM and FTS to critical systems with joint fluctuations of gapless fermions and bosons, but also propose a general criterion for the validity of the KZM and FTS with a gapless initial state. The general criterion, Eq. (6), can extend well beyond the scope of Dirac QCP. For instance, it was found that the density of excitations n_{ex} in the driven dynamics of the one dimensional spin chain with dispersion $E_k \propto \sqrt{c^2k^2 + k^4}$ shows the scaling

relation $n_{ex} \propto R^{1/3}$ under changing c linearly to cross its QCP at $c = 0$[32]. In this case, the low-energy mode of the gapless phase has the linear dispersion with $z' = 1$ and c is marginally irrelevant with zero scaling dimension. In contrast, near the QCP, the quadratic dispersion begins to dominate such that $z = 2$, and c becomes relevant with the scaling dimension of $1/\nu = 1$, which can be obtained by comparing the dimensions of c and k. Apparently, the criterion of Eq. (6) is fulfilled and n_{ex} satisfy the KZM of the QCP, i.e., $n \propto R^{d/r}$ with $d = 1$ and $r = 3$. In addition, Eq. (6) can also apply to the dynamic scaling in other QCPs[18,33], as discussed further in Supplementary Note 3.

From the application perspectives, we demonstrate that the nonequilibrium scaling form is capable of determining the critical exponents in Dirac QCP, providing an effective method to deciphering quantum critical properties in terms of driven dynamics. A large discrepancy in the critical exponents of the chiral Heisenberg universality class still exists despite extensive studies[42,49]. By directly fitting the curves of m^2 versus R in large R region with the power function for both DSM and AFM initial states, as shown in Fig. 2a and Figure 3a, respectively, we obtain $(2\beta/\nu r - d/r) = -0.26(1)$ and $2\beta/\nu r = 0.73(2)$. By setting $z = 1$, we obtain critical exponents $\nu = 0.98(4)$ and $\beta = 0.72(4)$, which are consistent with $\nu = 1.02(1)$ and $\beta = 0.76(2)$ from ref. 49 within error-bars. The detailed derivation and other ways to estimate critical exponents via FTS are shown in Supplementary Notes 4 and 5, and the corresponding results are shown in Supplementary Tables 1 and 2. It is important to note that equilibrium methods often require larger system sizes and careful finite-size scaling corrections to achieve comparable accuracy[49]. In contrast, in the framework of driven dynamics, the driven rate R constitutes a new tuning parameter. At large R, the impact of finite-size corrections is diminished, allowing for reliable critical exponent determination with relatively small system sizes. Moreover, the availability of diverse driving protocols with distinct FTS forms provides a compelling means to confirm the robustness and accuracy of these critical exponent determinations, as discussed further in Supplementary Note 5.

From experimental perspectives, driven dynamics is observed in cold-atom systems[11,20]. Due to recent developments in cold-atom-based quantum simulators of fermions[66–68], it is promising to detect driven dynamics in Dirac QCP and verify the generalized KZM and FTS as discussed in our study in these platforms. In real experiments, thermal fluctuations will inevitably enter. Thus, the scaling form should include $TR^{-z/r}$ as an additional variable in the full scaling form[26,69]. Nonetheless, as $T^{-1/z}$ plays similar roles as the system size in QCP, the scaling behaviors for large R are expected to be almost independent of T, in analogy to the finite-size cases. Physically, for large R, excitations induced by driving dominate over those induced by thermal fluctuations and therefore contribute the main dynamic scaling behaviors. Accordingly, it is foreseeable that the methodological approach developed here can be used to probe the critical properties in real experiments.

METHODS

Quantum Monte Carlo simulation of driven dynamics in imaginary-time direction

We have explored the driven dynamics of the Hubbard model (1) and the t-V model (4). Here, we elucidate the implementation of QMC to simulate the imaginary-time driven dynamics.

For models (1) and (4), we linearly vary the interaction strength $U(V)$ with imaginary time variable τ at the rate R as

$$U(\tau) = U_0 \pm R\tau, \tag{8}$$

$$V(\tau) = V_0 \pm R\tau, \tag{9}$$

where the $+$ ($-$) represents driving from disordered (ordered) initial state at $U_0(V_0)$. In our numerical simulation, for disordered initial state, we set $U_0 = 0$, $V_0 = 0$, while for ordered initial state we set $U_0 = 11.85$, $V_0 = 2.5$ far from the critical point.

The wave function $|\psi(\tau)\rangle$ obeys the imaginary-time Schrödinger equation[59]

$$-\frac{\partial}{\partial\tau}|\psi(\tau)\rangle = H(\tau)|\psi(\tau)\rangle. \tag{10}$$

The formal solution of Eq. (10) is given by $|\psi(\tau)\rangle = U(\tau, 0)|\psi(0)\rangle$ in which time evolution operator

$$U(\tau, 0) = \mathrm{T}\ \exp\left[-\int_0^\tau d\tau' H(\tau')\right], \tag{11}$$

with T being the time-ordering operator in imaginary-time direction. For the left vector $\langle\psi(\tau)| = \langle\psi(0)|U^\dagger(\tau, 0)$ with $U^\dagger(\tau, 0) = \overline{\mathrm{T}}\ \exp\left[-\int_0^\tau d\tau' H(\tau')\right]$, the Hermite conjugate simply changes the time-ordering operator T to an anti-time-ordering operator $\overline{\mathrm{T}}$. Since the model (1) and (4) is sign-problem-free and imaginary-time evolution does not induce additional sign problem, the imaginary-time dynamics of the models can be simulated by the determinant quantum Monte Carlo (DQMC) method.

To facilitate DQMC simulations of models (1) and (4), we begin by expressing the Hamiltonian in the form

$$H(\tau) = H_t + H_I(\tau), \tag{12}$$

where H_t represents the kinetic energy and $H_I(\tau)$ the interaction term, in which the interaction strength varies with τ. The initial state $|\psi(0)\rangle$ is the ground state of $H(0)$. In the DQMC simulation[56], the ground state of a given Hamiltonian is accessed by performing imaginary-time evolution on a trial wave function:

$$|\psi(0)\rangle = \lim_{\tau_0\to\infty} e^{-\tau_0 H(0)}|\psi_T\rangle, \tag{13}$$

where $|\psi_T\rangle$ is a Slater-determinant wave function generated as the ground state of the H_t. Consequently, for disordered DSM initial state $|\psi(0)\rangle = |\psi_T\rangle$, we set projection time $\tau_0 = 0$. For the AFM or CDW ordered initial state, a sufficiently long τ_0 is necessary to project the $|\psi_T$ onto the ground state of $H(0)$. In our simulations, we implement $\tau_0 = 120$ for the model (1), and $\tau_0 = 20$ for the model (4). We have numerically verified the convergence of our results with respect to increasing τ_0.

Following the standard DQMC methodology[56], we employ the Trotter decomposition to discretize imaginary time. Subsequently, we apply the Hubbard-Stratonovich (HS) transformation to decouple the fermion-fermion interaction, transforming it into a fermion bilinear form coupled to auxiliary fields. First, we perform Trotter decomposition on the process of imaginary-time evolution to generate initial state in (13):

$$|\psi(0)\rangle = \lim_{\Delta\tau\to 0}\prod_{n=1}^{N_{\tau_0}} e^{-\Delta\tau H_t}e^{-\Delta\tau H_I(0)}|\psi_T\rangle, \tag{14}$$

where $\Delta\tau$ is the imaginary-time Trotter time defined by $\Delta\tau = \tau_0/N_{\tau_0}$.

Similarly, the Trotter decomposition in driven dynamics is expressed as

$$\mathrm{T}\ \exp\left[-\int_0^\tau d\tau' H(\tau')\right] = \lim_{\Delta\tau\to 0}\prod_{n=1}^{N_\tau}\left[\mathrm{e}^{-\Delta\tau H_t}\mathrm{e}^{-\Delta\tau H_I(\tau_n)}\right], \tag{15}$$

where the Trotter time is defined as $\Delta\tau = \tau/N_\tau$, with with N_τ the number of time slices and $\tau_n = n\Delta\tau$. Combining these two parts, the wave function $|\psi(\tau)\rangle$ is expressed as:

$$|\psi(\tau)\rangle = U(\tau,0)P_G|\psi_T\rangle, \tag{16}$$

where $U(\tau,0) = \lim_{\Delta\tau\to 0}\prod_{n=1}^{N_\tau}\left[e^{-\Delta\tau H_t}e^{-\Delta\tau H_I(\tau_n)}\right]$ and $P_G = \lim_{\Delta\tau\to 0}\prod_{n=1}^{N_{\tau_0}}\left[e^{-\Delta\tau H_t}e^{-\Delta\tau H_I(0)}\right]$. In our practical implementation, we choose $\Delta\tau = 0.05$ in both (14) and (15). We have numerically confirmed that $\Delta\tau = 0.05$ is sufficiently small to guarantee that the time-step error introduced by the Trotter decomposition is negligible, with the details shown in the Supplementary Note 6.

Next, we apply the HS transformation to decouple the interacting part $H_I(\tau)$ in models (1) and (4). For the Hubbard interaction in (1):

$$e^{-\frac{\Delta\tau U(\tau_n)}{2}(n_{i\uparrow}+n_{i\downarrow}-1)^2} = \sum_{l_{i,\tau_n}=\pm1,\pm2}\gamma(l_{i,\tau_n})e^{i\sqrt{\frac{\Delta\tau U(\tau_n)}{2}}\eta(l_{i,\tau_n})(n_{i\uparrow}+n_{i\downarrow}-1)}, \tag{17}$$

and for the density interaction in (4):

$$e^{-\frac{\Delta\tau V(\tau_n)}{2}\left(c_i^\dagger c_j + c_j^\dagger c_i\right)^2} = \sum_{l_{i,\tau_n}=\pm1,\pm2}\gamma(l_{i,\tau_n})e^{i\sqrt{\frac{\Delta\tau V(\tau_n)}{2}}\eta(l_{i,\tau_n})\left(c_i^\dagger c_j + c_j^\dagger c_i\right)}, \tag{18}$$

where the four-component space-time auxiliary fields γ and η take the following values:

$$\gamma(\pm1) = 1+\sqrt{6}/3, \gamma(\pm2) = 1-\sqrt{6}/3, \tag{19}$$

$$\eta(\pm1) = \pm\sqrt{2\left(3-\sqrt{6}\right)}, \eta(\pm2) = \pm\sqrt{2\left(3+\sqrt{6}\right)}. \tag{20}$$

Subsequent to the procedures outlined above, both the imaginary-time evolution operator $U(\tau, 0)$ and the generator of the initial state P_G can be expressed as products of exponentials of fermion bilinear operators. This representation significantly simplifies calculations, enabling the straightforward determination of wavefunction overlaps under imaginary-time evolution $\langle\psi(\tau)|\psi(\tau)\rangle$ and the expectation values of observables $\langle O(\tau)| = \rangle\frac{\langle\psi(\tau)|O|\psi(\tau)\rangle}{\langle\psi(\tau)|\psi(\tau)\rangle}$ in the framework of conventional DQMC[56].

For updating the auxiliary fields, we employ a local update scheme, sequentially updating the field at each site and time slice. In non-equilibrium simulations, one Markov chain consists of N_{sweep} iterations. Each iteration involves updating all sites across all time slices, resulting in a total of $N_{\text{sweep}}(N_\tau + N_{\tau_0})N_{\text{site}}$ Monte Carlo updates per chain, where N_{sweep} typically ranges from 10^2 to 10^3. Here, N_{site} represents the number of lattice sites. To ensure thermalization, we perform an initial equilibration of 5 sweeps before taking measurements. Finally, for each data point, we typically run two independent Markov chains to improve statistical sampling.

Data availability

The research data generated in this study have been deposited in the Figshare database under accession code https://doi.org/10.6084/m9.figshare.29207942.

Code availability

All numerical codes in this paper are available upon request to the corresponding authors (Zi-Xiang Li and Shuai Yin).

References

1. Dziarmaga, J. Dynamics of a quantum phase transition and relaxation to a steady state. *Adv. Phys.* **59**, 1063–1189 (2010).
2. Polkovnikov, A., Sengupta, K., Silva, A. & Vengalattore, M. Colloquium: Nonequilibrium dynamics of closed interacting quantum systems. *Rev. Mod. Phys.* **83**, 863–883 (2011).
3. Kibble, T. W. B. Topology of cosmic domains and strings. *J. Phys. A: Math. Gen.* **9**, 1387 (1976).
4. Zurek, W. H. Cosmological experiments in superfluid helium? *Nature* **317**, 505–508 (1985).
5. Zurek, W. H., Dorner, U. & Zoller, P. Dynamics of a quantum phase transition. *Phys. Rev. Lett.* **95**, 105701 (2005).
6. Dziarmaga, J. Dynamics of a quantum phase transition: exact solution of the quantum Ising model. *Phys. Rev. Lett.* **95**, 245701 (2005).
7. Polkovnikov, A. Universal adiabatic dynamics in the vicinity of a quantum critical point. *Phys. Rev. B* **72**, 161201 (2005).
8. Du, K. et al. Kibble-Zurek mechanism of Ising domains. *Nat. Phys.* **19**, 1495–1501 (2023).
9. Ko, B., Park, J. W. & Shin, Y. Kibble-Zurek universality in a strongly interacting fermi superfluid. *Nat. Phys.* **15**, 1227–1231 (2019).
10. Maegochi, S., Ienaga, K. & Okuma, S. Kibble-Zurek mechanism for dynamical ordering in a driven vortex system. *Phys. Rev. Lett.* **129**, 227001 (2022).
11. Keesling, A. et al. Quantum kibble-Zurek mechanism and critical dynamics on a programmable Rydberg simulator. *Nature* **568**, 207–211 (2019).
12. Ebadi, S. et al. Quantum phases of matter on a 256-atom programmable quantum simulator. *Nature* **595**, 227–232 (2021).
13. Qiu, L.-Y. et al. Observation of generalized Kibble-Zurek mechanism across a first-order quantum phase transition in a spinor condensate. *Sci. Adv.* **6**, eaba7292 (2020).
14. Ebadi, S. et al. Quantum optimization of maximum independent set using Rydberg atom arrays. *Science* **376**, 1209–1215 (2022).
15. Sunami, S. et al. Universal scaling of the dynamic BKT transition in quenched 2d bose gases. *Science* **382**, 443–447 (2023).
16. Li, B.-W. et al. Probing critical behavior of long-range transverse-field Ising model through quantum Kibble-Zurek mechanism. *PRX Quantum* **4**, 010302 (2023).
17. Zhong, F. & Xu, Z. Dynamic Monte Carlo renormalization group determination of critical exponents with linearly changing temperature. *Phys. Rev. B* **71**, 132402 (2005).
18. Deng, S., Ortiz, G. & Viola, L. Dynamical non-ergodic scaling in continuous finite-order quantum phase transitions. *Europhys. Lett.* **84**, 67008 (2009).
19. Chandran, A., Erez, A., Gubser, S. S. & Sondhi, S. L. Kibble-Zurek problem: Universality and the scaling limit. *Phys. Rev. B* **86**, 064304 (2012).
20. Clark, L. W., Feng, L. & Chin, C. Universal space-time scaling symmetry in the dynamics of bosons across a quantum phase transition. *Science* **354**, 606–610 (2016).
21. Kolodrubetz, M., Clark, B. K. & Huse, D. A. Nonequilibrium dynamic critical scaling of the quantum Ising chain. *Phys. Rev. Lett.* **109**, 015701 (2012).
22. Gong, S., Zhong, F., Huang, X. & Fan, S. Finite-time scaling via linear driving. *N. J. Phys.* **12**, 043036 (2010).
23. Feng, B., Yin, S. & Zhong, F. Theory of driven nonequilibrium critical phenomena. *Phys. Rev. B* **94**, 144103 (2016).
24. Huang, Y., Yin, S., Feng, B. & Zhong, F. Kibble-Zurek mechanism and finite-time scaling. *Phys. Rev. B* **90**, 134108 (2014).
25. Liu, C.-W., Polkovnikov, A. & Sandvik, A. W. Dynamic scaling at classical phase transitions approached through nonequilibrium quenching. *Phys. Rev. B* **89**, 054307 (2014).
26. Yin, S., Mai, P. & Zhong, F. Nonequilibrium quantum criticality in open systems: the dissipation rate as an additional indispensable scaling variable. *Phys. Rev. B* **89**, 094108 (2014).

27. Liu, C.-W., Polkovnikov, A. & Sandvik, A. W. Quantum versus classical annealing: Insights from scaling theory and results for spin glasses on 3-regular graphs. *Phys. Rev. Lett.* **114**, 147203 (2015).
28. King, A. D. et al. Quantum critical dynamics in a 5,000-qubit programmable spin glass. *Nature* **617**, 61–66 (2023).
29. Garcia, J. S. & Chepiga, N. Resolving chiral transitions in one-dimensional Rydberg arrays with quantum Kibble-Zurek mechanism and finite-time scaling. *Phys. Rev. B* **110**, 125113 (2024).
30. Dupont, M. & Moore, J. E. Quantum criticality using a superconducting quantum processor. *Phys. Rev. B* **106**, L041109 (2022).
31. Polkovnikov, A. & Gritsev, V. Breakdown of the adiabatic limit in low-dimensional gapless systems. *Nat. Phys.* **4**, 477–481 (2008).
32. Divakaran, U., Dutta, A. & Sen, D. Quenching along a gapless line: a different exponent for defect density. *Phys. Rev. B* **78**, 144301 (2008).
33. Suzuki, S. & Dutta, A. Universal scaling for a quantum discontinuity critical point and quantum quenches. *Phys. Rev. B* **92**, 064419 (2015).
34. Gross, D. J. & Neveu, A. Dynamical symmetry breaking in asymptotically free field theories. *Phys. Rev. D.* **10**, 3235–3253 (1974).
35. Gracey, J. A., Luthe, T. & Schröder, Y. Four loop renormalization of the Gross-Neveu model. *Phys. Rev. D.* **94**, 125028 (2016).
36. Poland, D., Rychkov, S. & Vichi, A. The conformal bootstrap: Theory, numerical techniques, and applications. *Rev. Mod. Phys.* **91**, 015002 (2019).
37. You, Y.-Z., He, Y.-C., Xu, C. & Vishwanath, A. Symmetric fermion mass generation as deconfined quantum criticality. *Phys. Rev. X* **8**, 011026 (2018).
38. Castro Neto, A. H., Guinea, F., Peres, N. M. R., Novoselov, K. S. & Geim, A. K. The electronic properties of graphene. *Rev. Mod. Phys.* **81**, 109–162 (2009).
39. Hasan, M. Z. & Kane, C. L. Colloquium: Topological insulators. *Rev. Mod. Phys.* **82**, 3045–3067 (2010).
40. Qi, X.-L. & Zhang, S.-C. Topological insulators and superconductors. *Rev. Mod. Phys.* **83**, 1057–1110 (2011).
41. Janssen, L. & Herbut, I. F. Antiferromagnetic critical point on graphene's honeycomb lattice: a functional renormalization group approach. *Phys. Rev. B* **89**, 205403 (2014).
42. Parisen Toldin, F., Hohenadler, M., Assaad, F. F. & Herbut, I. F. Fermionic quantum criticality in honeycomb and π-flux Hubbard models: Finite-size scaling of renormalization-group-invariant observables from quantum Monte Carlo. *Phys. Rev. B* **91**, 165108 (2015).
43. Li, Z.-X., Vaezi, A., Mendl, C. B. & Yao, H. Numerical observation of emergent spacetime supersymmetry at quantum criticality. *Sci. Adv.* **4**, eaau1463 (2018).
44. Tabatabaei, S. M., Negari, A.-R., Maciejko, J. & Vaezi, A. Chiral Ising Gross-Neveu criticality of a single Dirac cone: a quantum Monte Carlo study. *Phys. Rev. Lett.* **128**, 225701 (2022).
45. Otsuka, Y., Seki, K., Sorella, S. & Yunoki, S. Quantum criticality in the metal-superconductor transition of interacting Dirac fermions on a triangular lattice. *Phys. Rev. B* **98**, 035126 (2018).
46. Sorella, S. & Tosatti, E. Semi-metal-insulator transition of the Hubbard model in the honeycomb lattice. *Europhys. Lett.* **19**, 699 (1992).
47. Herbut, I. F. Interactions and phase transitions on graphene's honeycomb lattice. *Phys. Rev. Lett.* **97**, 146401 (2006).
48. Assaad, F. F. & Herbut, I. F. Pinning the order: The nature of quantum criticality in the Kubbard model on honeycomb lattice. *Phys. Rev. X* **3**, 031010 (2013).
49. Otsuka, Y., Yunoki, S. & Sorella, S. Universal quantum criticality in the metal-insulator transition of two-dimensional interacting Dirac electrons. *Phys. Rev. X* **6**, 011029 (2016).
50. Wang, L., Corboz, P. & Troyer, M. Fermionic quantum critical point of spinless fermions on a honeycomb lattice. *N. J. Phys.* **16**, 103008 (2014).
51. Li, Z.-X., Jiang, Y.-F. & Yao, H. Fermion-sign-free Majarana-quantum-Monte-Carlo studies of quantum critical phenomena of Dirac fermions in two dimensions. *N. J. Phys.* **17**, 085003 (2015).
52. Li, Z.-X., Jiang, Y.-F., Jian, S.-K. & Yao, H. Fermion-induced quantum critical points. *Nat. Commun.* **8**, 314 (2017).
53. Dutta, A., Singh, R. R. P. & Divakaran, U. Quenching through Dirac and semi-Dirac points in optical lattices: Kibble-Zurek scaling for anisotropic quantum critical systems. *Europhysics Letters* **89**, 67001 (2009).
54. Sun, Z., Deng, M. & Li, F. Kibble-Zurek behavior in one-dimensional disordered topological insulators. *Phys. Rev. B* **106**, 134203 (2022).
55. Deng, M., Sun, Z. & Li, F. Defect production across higher-order phase transitions beyond Kibble-Zurek scaling. *Phys. Rev. Lett.* **134**, 010409 (2025).
56. Assaad, F. & Evertz, H. *World-line and Determinantal Quantum Monte Carlo Methods for Spins, Phonons and Electrons*, 277–356 (Springer Berlin, Heidelberg, 2008).
57. Li, Z.-X. & Yao, H. Sign-problem-free fermionic quantum Monte Carlo: Developments and applications. *Annu. Rev. Condens. Matter Phys.* **10**, 337–356 (2019).
58. Schmitt, M., Rams, M. M., Dziarmaga, J., Heyl, M. & Zurek, W. H. Quantum phase transition dynamics in the two-dimensional transverse-field Ising model. *Sci. Adv.* **8**, eabl6850 (2022).
59. De Grandi, C., Polkovnikov, A. & Sandvik, A. W. Universal nonequilibrium quantum dynamics in imaginary time. *Phys. Rev. B* **84**, 224303 (2011).
60. Hesselmann, S. & Wessel, S. Thermal Ising transitions in the vicinity of two-dimensional quantum critical points. *Phys. Rev. B* **93**, 155157 (2016).
61. Li, Z.-X., Jiang, Y.-F. & Yao, H. Solving the fermion sign problem in quantum Monte Carlo simulations by Majorana representation. *Phys. Rev. B* **91**, 241117 (2015).
62. Li, Z.-X., Jiang, Y.-F. & Yao, H. Majorana-time-reversal symmetries: a fundamental principle for sign-problem-free quantum Monte Carlo simulations. *Phys. Rev. Lett.* **117**, 267002 (2016).
63. Wei, Z. C., Wu, C., Li, Y., Zhang, S. & Xiang, T. Majorana positivity and the fermion sign problem of quantum Monte Carlo simulations. *Phys. Rev. Lett.* **116**, 250601 (2016).
64. Herbut, I. F., Juričić, V. & Vafek, O. Relativistic Mott criticality in graphene. *Phys. Rev. B* **80**, 075432 (2009).
65. Tang, H.-K. et al. The role of electron-electron interactions in two-dimensional Dirac fermions. *Science* **361**, 570–574 (2018).
66. Jördens, R., Strohmaier, N., Günter, K., Moritz, H. & Esslinger, T. A mott insulator of fermionic atoms in an optical lattice. *Nature* **455**, 204–207 (2008).
67. Mazurenko, A. et al. A cold-atom fermi–Hubbard antiferromagnet. *Nature* **545**, 462–466 (2017).
68. Venu, V. et al. Unitary p-wave interactions between fermions in an optical lattice. *Nature* **613**, 262–267 (2023).
69. Yin, S., Lo, C.-Y. & Chen, P. Scaling in driven dynamics starting in the vicinity of a quantum critical point. *Phys. Rev. B* **94**, 064302 (2016).

Acknowledgements

We would like to thank A. W. Sandvik and F. Zhong for helpful discussions. This work was supported by the National Natural Science Foundation of China (Nos. 12222515 and 12075324 to Z.Z., Y.K.Y, Zhi-Xuan Li and S.Y., No. 12347107 and No. 12474146 to Zi-Xiang Li), the Science and Technology Projects in Guangdong Province (No. 2021QN02X561 to S.Y.), and the Science and Technology Projects in Guangzhou City (No. 2025A04J5408 to S.Y.). The authors would like to thank the National Supercomputer Center in Guangzhou for providing high-performance computational resources.

Author contributions

S.Y. and Z.X.L. conceived the project and planned the study. The numerical simulations were carried out by Z.Z., Y.Y.K. and Z.X.L. All authors contributed to the scaling analyses.

Competing interests

The authors declare no competing interests.

Additional information

Supplementary information The online version contains supplementary material available at https://doi.org/10.1038/s41467-025-61611-6.

Correspondence and requests for materials should be addressed to Zi-Xiang Li or Shuai Yin.

Peer review information *Nature Communications* thanks Michele Casula, Sei Suzuki and the other, anonymous, reviewer(s) for their contribution to the peer review of this work. A peer review file is available.